

Experimental Investigation on Frequency Characteristics of Plasma Synthetic Jets

Zong, H.; Kotsonis, Marios

Publication date

2017

Document Version

Accepted author manuscript

Published in

Physics of Fluids

Citation (APA)

Zong, H., & Kotsonis, M. (2017). Experimental Investigation on Frequency Characteristics of Plasma Synthetic Jets. *Physics of Fluids*, 29(11).

Important note

To cite this publication, please use the final published version (if applicable).
Please check the document version above.

Copyright

Other than for strictly personal use, it is not permitted to download, forward or distribute the text or part of it, without the consent of the author(s) and/or copyright holder(s), unless the work is under an open content license such as Creative Commons.

Takedown policy

Please contact us and provide details if you believe this document breaches copyrights.
We will remove access to the work immediately and investigate your claim.

Experimental Investigation on Frequency Characteristics of Plasma Synthetic Jets

Haohua Zong* and Marios Kotsonis

Faculty of Aerospace Engineering, Delft University of Technology, Delft 2629 HS, Netherlands

Abstract: The performance of a two-electrode plasma synthetic jet actuator (PSJA) is investigated for a wide range of dimensionless actuation frequencies (f^*) using high-speed phase-locked Particle Imaging Velocimetry (PIV) measurements. The jet-induced velocity fields in the axisymmetric plane are measured during both transient and steady working stages of the PSJA. When f^* increases, the jet duration time (T_{jet}) is reduced while the peak suction velocity (U_s) increases consistently. Three integral parameters, including the total expelled gas mass, impulse and issued mechanical energy also decline considerably with increasing frequency, which is shown to relate to both the reduced cavity density and the decreasing jet duration. Theoretical analysis reveals that the mean cavity density decreases monotonically with the square root of discharge frequency. The decreasing rate is inversely proportional to a thermal cut-off frequency (f_c , 210Hz for the current study), which scales with the convective heat transfer coefficient between the actuator cavity walls and the cavity gas, as well as the area of the cavity internal surface. In the time-averaged velocity fields, the jet centreline velocity (\bar{U}_c) exhibits a local maximum in the axial coordinate. The nondimensional maximum centreline velocity reduces with increasing frequency of operation. The jet spreading rate of the plasma synthetic jets (PSJ) decreases from 0.14 to 0.09 with increasing frequency. During the transient working stage of PSJ, the exit velocity trace elapses 20 successive actuation cycles to stabilize. In contrast to the exit velocity, approximately 130 cycles are needed for the mean cavity density/temperature to reach steady values.

Keywords: plasma; synthetic jet; actuator; frequency effect; characteristics;

I. INTRODUCTION

Plasma flow control (PFC) has received an overwhelming attention from the flow control community in the past 15 years due to its intrinsic rapid response ($O(1 \mu\text{s})$), high bandwidth (10-100 kHz) and simple construction (Corke, Enloe & Wilkinson, 2010; Cattafesta & Sheplak, 2011). Application prospects of PFC include, but are not limited to, boundary layer transition control (Grundmann & Tropea, 2007), lift augmentation/ drag reduction (Post & Corke, 2004), shock wave/ boundary interaction control (Narayanaswamy, Raja & Clemens, 2012; Greene et al. 2015), noise mitigation (Thomas, Kozlov & Corke, 2008; Samimy et al., 2007) and so on. Effective flow control relies on the appropriate selection of actuators. Compared with surface dielectric barrier discharge actuators and arc plasma actuators, plasma synthetic jet actuators (PSJAs) proposed by Grossman, Bohdan & VanWie (2003) are capable of generating high-velocity (300 m/s) high-frequency (5 kHz) pulsed jets with acceptable power level ($O(100 \text{ W})$), thus tailored for high-Reynolds-number, high-velocity flow control (Narayanaswamy, Raja & Clemens, 2010).

For a ramp-induced shock wave/boundary layer interaction in a Mach 3 flow, plasma synthetic jets (PSJs) issued at a Strouhal number of 0.04 are able to decrease the overall amplitude of the low-frequency pressure fluctuations by 30% (Narayanaswamy, Raja & Clemens, 2012). In a similar setup (Strouhal number: 0.014), the size of the separation region reduces by up to 40% and the integrated momentum of the downstream attached boundary layer is significantly increased by PSJs pitched at 20 degrees (Greene et al. 2015). Emerick et al. (2014) used a PSJA array (Sparkjet array in their paper) to impinge a Mach 1.5 crossflow, and a maximum flow deflection angle of 5 degrees was created in both single-shot and burst modes. These results are promising however limited to the laboratory scale. Further improvements in the control effect require elucidation of the complex working mechanism and optimization of the actuator geometries. The factors influencing the performance of PSJAs can be classified into two categories, namely, 'electrical' and 'geometrical'.

Pertinent electrical parameters mainly refer to discharge energy, frequency, discharge type, duration etc. Theoretical analysis and experimental observations have shown that as the nondimensional energy deposition increases, the peak jet velocity, jet duration time and electro-mechanical efficiency increase substantially (Anderson & Knight, 2012; Zong et al., 2015a; Wang et al., 2013; Reedy et al., 2013). In repetitive operation mode, the total pressure of the pulsed jet deteriorates with increasing frequency as a result of reduced cavity density and increasing cavity temperature (Belinger et al. 2011; Zong et al. 2015b). Three main strategies exist for feeding the PSJA, namely, nanosecond pulse discharge, capacitive discharge and pulsed DC discharge. Nanosecond pulse discharge features a high heating-efficiency ($>60\%$) due to the large reduced electric field (electric field over particle concentration, E/N) (Zhu et al., 2014; Xu et al., 2014). However, the low pulse energy ($O(\text{mJ})$) caused by the ultra-short discharge duration confines its application to small-volume PSJA ($<100 \text{ mm}^3$). In contrast to nanosecond pulse discharge, the pulse energy of capacitive discharge can be tuned within a wide range (0.01 J-10 J) whereas the heating efficiency is demonstrated to be lower than 10% (Belinger et al., 2014; Golbabaie-Asl, knight & Wilkinson, 2014). Finally, pulsed DC discharge exhibits the advantage of adaptable discharge duration, however its discharge efficiency is considerably low due to the inevitable current-limiting resistor (Zong et al. 2016a; Narayanaswamy, Raja & Clemens, 2010).

The pertinent geometrical parameters include the exit orifice diameter/ shape, cavity volume, electrode distance etc. As orifice diameter increases, the jet duration time decreases while peak jet velocity and jet mechanical energy remain unchanged (Zong & Kotsonis, 2016b). The effect of the cavity volume on the performance of PSJA is essentially incorporated by the nondimensional energy deposition. A large cavity volume leads to a long-duration yet low-velocity pulsed jet (Cybyk, Grossman & Van Wie, 2003). Electrode distance is closely related to the heating volume and the heating efficiency. With constant energy deposition and increasing electrode distance, both the peak jet velocity and jet duration time increase monotonically (Zong et al. 2016a).

As summarized, considerable investigations of the characteristics of PSJA are available to guide the optimal design of the actuator geometry. Nevertheless, the majority of these studies (especially frequency characteristics) are based on schlieren imaging and pressure measurements (Belinger et al. 2011; Zong et al. 2015b; Chiatto & de Luca, 2017) which largely limits our current understanding of the underlying mechanism. Direct comparison has shown that the peak jet velocity determined by tracking the propagating features (jet front, front vortex ring) in schlieren images is only half of the peak exit velocity measured by Particle Imaging Velocimetry (PIV) (Zong & Kotsonis, 2017a). Similarly, the velocity estimated from the total pressure measurements based on incompressible flow relations also severely underestimates the real jet exit velocity, as the jet density can be less than 70% of the ambient density even in single-shot operation mode (Zong & Kotsonis, 2016b).

In flow control applications, working frequency of the PSJA is directly related to the Strouhal number, thus serving as one of the most important actuation parameters. Whereas to the authors' knowledge, the influence of actuation frequency on crucial performance parameters of the PSJ such as peak jet velocity, jet duration time and jet spreading rate are largely unclear. This also applies for the transient working mechanism during repetitive operation (namely the start-up process). The present study provides an effort to fill this gap. A high-speed phase-locked planar PIV system is deployed to measure the jet induced velocity fields in the axisymmetric plane in a wide range of actuation frequencies (50 Hz-1429 Hz). Detailed description of the experiment setup is provided in Section II. The effect of frequency on performance characteristics of PSJA are investigated using both phase-averaging and time-averaging in Section III. The transient working mechanism is revealed in Section IV with the support of both experimental data and theoretical energy equilibrium analysis.

II. EXPERIMENTAL SETUP

2.1 Actuator and power supply

For the purposes of this investigation a two-electrode actuator is constructed and mainly consists of a cubic ceramic shell (dimension: $15 \times 15 \times 15 \text{ mm}^3$) and a flat-plate cap, which are made of machinable glass ceramic (MACOR) and can be assembled together through a step groove (Figure 1 (a)). A cylindrical cavity resides in the cubic ceramic shell. The diameter and height of this ceramic cavity are 10 mm and 12 mm respectively, resulting in a cavity volume (V_{ca}) of 942 mm^3 . Three round holes (diameter: 1.1 mm) are drilled in the centres of the two side walls and the bottom surface, respectively. Two tungsten needles are inserted into the two side holes, serving as anode and cathode respectively. The remaining bottom hole is connected with a capillary tube (inner diameter: 0.4 mm), which seeds the tracer particles necessary for PIV measurements. The distance between the anode and

the cathode are fixed at 3 mm. On the ceramic cap, a round orifice (diameter: $D=1.5$ mm; throat length: $L_{th}=3$ mm) is created and serves as the jet exit. In the centre of the jet exit, a cylindrical coordinate system is established, with r -axis and x -axis along axial and radial direction respectively.

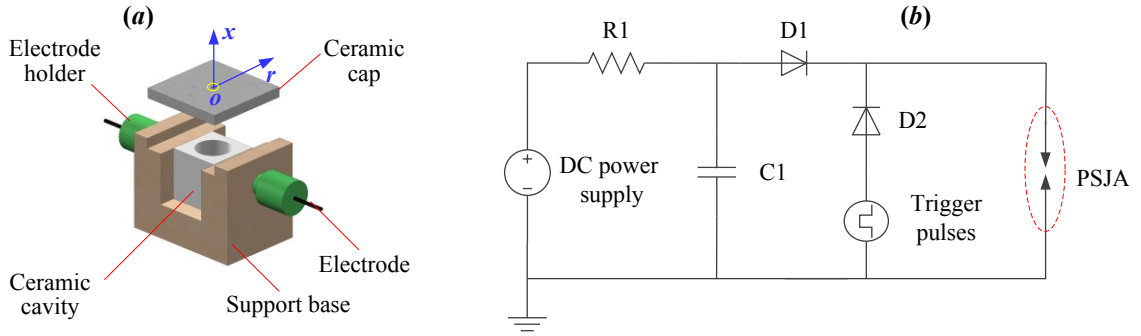


Figure 1 (a) Actuator components and (b) power supply system. Jet exit is indicated by a yellow circle.

A sequential discharge (trigger discharge-capacitive discharge) power supply is adopted to feed the two-electrode actuator, as shown in Figure 1 (b), based on previous three-electrode implementations used in Zong & Kotsonis (2016a). However, compared to the power supply used in Zong & Kotsonis (2016a), the circuit structure is largely simplified since the trigger function is realized by the anode instead of an additional trigger electrode. A DC power supply (output voltage: $U_0=2$ kV; power: 2 kW), a resistor ($R1$, resistance: 1.5 k Ω ; power: 200 W) and an energy-storing capacitor ($C1$, capacitance: $C_1=0.1$ μ F) constitute the charging circuit. High-voltage trigger pulses (amplitude: 10 kV; width: 100 μ s) are generated by a high-voltage amplifier (Trek Model, 20/20C) to break the electrode gap. Immediately after breakdown, the energy stored in $C1$ is rapidly released into the discharge channel in the form of arc heating. Two high-voltage diodes ($D1$ and $D2$) isolate the capacitive-discharge circuit and the trigger-discharge circuit from each other to ensure protection from back-current overloading.

2.2 PIV measurement scheme

A high-speed phase-locked PIV system is employed to measure the ensuing jet-induced velocity fields in the axisymmetric plane, consisting of a high-speed laser (Continuum Mesa PIV, 532-120-M), a high-speed camera (Photron, Fastcam SA-1, resolution: 1024 \times 1024 pixels) and a programmable timing unit (PTU) (LaVision, HSC). To ensure quiescent flow conditions, the actuator is placed in a closed plexiglass box. Dielectric mineral oil particles are delivered into both the actuator cavity and the plexiglass box through an atomizer (TSI, 9302). Prior to discharge ignition, the intra-cavity seeding is switched off to avoid possible interferences on the jet flow. The laser beam is shaped into a thin sheet (thickness: approximately 0.6 mm) by two spherical lenses and one cylindrical lens. The laser sheet is kept strictly vertical, passing through xr -plane. A 200 mm macro lens (Nikon, Micro-Nikkor) and an extension tube (36 mm) are mounted on the high-speed camera to image a field of view of 12 mm \times 12 mm ($8D\times 8D$), achieving a magnification factor of 1.7. Davis 8.3.1 is used to process the recorded data set. The final interrogation window size and overlapping ratio used in PIV cross-correlation are 24 \times 24 and 75% respectively, leading to a final spatial resolution of 0.07 mm/vector.

Raw images are recorded in double frame mode, synchronized with the discharge ignition. The time delay between discharge ignition and image recording (t , namely the phase) is adjusted by a digital delay/pulse generator (Stanford Research Systems, DG535) in high accuracy ($< 1 \mu\text{s}$). Six cases with increasing discharge frequency and constant energy deposition are tested, as listed in Table 1. For each case, approximately 30-70 phases are selected to execute the PIV measurement. Time steps between adjacent phases range from $25 \mu\text{s}$ to 1ms , depending on the peak flow velocity. For each phase, one long sequence containing 200 successive pulses is recorded.

As noticed by Sary et al. (2014) and Zong et al. (2015b), the first several pulses (less than 20) after the PSJA starts up lie in transient working stage with unstable performance, while the later pulses in steady working stage. Specifically, in the transient working stage, the cavity density and cavity temperature exhibit a stair-stepping variation and the peak jet velocity varies from cycle to cycle. By contrast, the steady stage features a periodical variation of the exit velocity, cavity density as well as cavity temperature. The transient stage during repetitive operation is inevitable and will transition to the steady stage once two conditions are met. First, the mass ejected through the exit orifice in one cycle should be counteracted by that ingested into the cavity (cavity mass conservation). Second, the cycle work done by the PSJA should be balanced by the net heat exchange between the environment and the actuator during one period (The first law of thermodynamics). Out of this consideration, only the last 100 snapshots of each sequence are adopted to get statistically-averaged steady-stage performance of the PSJA. Preliminary convergence study has verified that this sampling size (100) is enough to get statistically-converged mean flow fields. Additionally, Case 6 is selected to reveal the transient working mechanism due to the most significant frequency effect. For each phase of this case, 20 short sequences incorporating the snapshots of the first 50 pulses are recorded.

The uncertainty in phase-locked PIV measurements has been discussed in detail in Zong & Kotsonis (2017a and 2017b). The finite ensemble size, peak locking errors, finite laser sheet thickness and discharge timing uncertainty are identified as the four main sources of velocity measurement error. Following a similar procedure, the total measurement uncertainty is computed to be less than 5% of the peak jet velocity.

Table 1. Discharge parameters for all cases

| Cases | f_d (Hz) | T_d (ms) | f^* | ε |
|--------|------------|------------|-------|---------------|
| Case 1 | 50 | 20 | 0.037 | 0.84 |
| Case 2 | 100 | 10 | 0.074 | 0.84 |
| Case 3 | 200 | 5 | 0.148 | 0.84 |
| Case 4 | 500 | 2 | 0.370 | 0.84 |
| Case 5 | 1000 | 1 | 0.739 | 0.84 |
| Case 6 | 1429 | 0.7 | 1.056 | 0.84 |

It should be noted that the peak test frequency (1429 Hz) in this study is actually limited by the characteristic time of the charging circuit ($\tau=0.15 \text{ms}$). To fully restore the energy-storing capacitor (criterion: capacitor voltage reaches 99% of the DC voltage), 4.67 times of τ (namely 0.7ms) are necessary, corresponding to an odd frequency value of 1429 Hz. Based on the cavity size and ambient conditions, the Helmholtz natural frequency (f_h) of the PSJA is computed and further used to normalize the discharge frequency (Chiutto & de Luca, 2017), resulting in a nondimensional

frequency (f^*) as shown in Equation (1). P_0 and ρ_0 are atmospheric pressure and density respectively. A_e denotes area of the exit orifice.

$$\begin{cases} f_h = \frac{1}{2\pi} \sqrt{\frac{\gamma P_0}{\rho_0}} \sqrt{\frac{A_e}{V_{ca} L_{th}}} \\ f^* = \frac{f_d}{f_h} \end{cases} \quad (1)$$

As interpreted in Chiatto & de Luca (2017), f_h (1353 Hz for the actuator used in this study) is essentially the alternation frequency between the jet and the refresh stages within one cycle. Since at least one alternation is needed to reset the actuator, f_h can be interpreted as the theoretical limit working frequency of the PSJA. The nondimensional energy deposition (ε) is defined as the ratio of capacitor energy to the initial internal energy of the cavity gas, as follows,

$$\varepsilon = \frac{E_c}{E_g} = \frac{0.5 \cdot C_1 U_0^2}{C_v \rho_0 V_{ca} T_0} \quad (2)$$

Where, C_v is the constant-volume specific heat capacity; T_0 represent ambient temperature. For the tested cases, ε remains at 0.84 while f^* ranges from 0.037 to 1.056.

III. STEADY-STAGE PERFORMANCE

This section presents results and analysis pertaining to the steady-stage operation of the actuator. In Section 3.1, the spatially-averaged exit velocity and jet penetration length extracted from phase-averaged velocity fields are first analysed. Subsequently, integral parameters pertaining to a single pulsed jet cycle including the expelled gas mass, impulse and issued mechanical energy are evaluated based on a simplified model proposed by Zong & Kotsonis (2016b). Finally, the effect of frequency on the jet centreline velocity decay and jet spreading rate is analysed in Section 3.2 based on time-average velocity fields.

3.1 Phase-averaged results at steady working stage

A. Jet penetration length and exit velocity

Phase-averaged velocity fields for the lowest frequency case (Case 1, $f^*=0.037$) and the highest frequency case (Case 6, $f^*=1.056$) are shown in Figure 2. In the case of $f^*=0.037$, a bow-shape velocity structure, in the vicinity of the jet exit, is formed at $t=50\mu s$. Zong & Kotsonis (2016a) have shown that such structure is the result of multiple shock waves, spatially smoothed by the phase averaging procedure. These shock waves are caused by the rapid heating of the pulsed arc and can be used to trigger the instability in the shear layers of high-subsonic jets (Chedevergne et al., 2015). Pulsed jets with peak velocity of up to 70 m/s are released after these shock waves, creating a hammer-shape jet body. In this upstanding jet body, several discrete high-velocity cores can be observed (Figure 1 (b)-(c)), as a result of the self-induction effect of shear-layer vortex rings (Wu, Ma & Zhou, 2007). The axial spacing between these high-velocity cores grows approximately from $2D$ at $t=250\mu s$ to $3D$ at $t=500\mu s$. After the jet stage ceases, fresh ambient air near the exit orifice ($-1 < r/D < 1$, $x/D < 1$) is ingested into the actuator cavity at low velocity, mixing with the high-temperature low-density residual cavity gas.

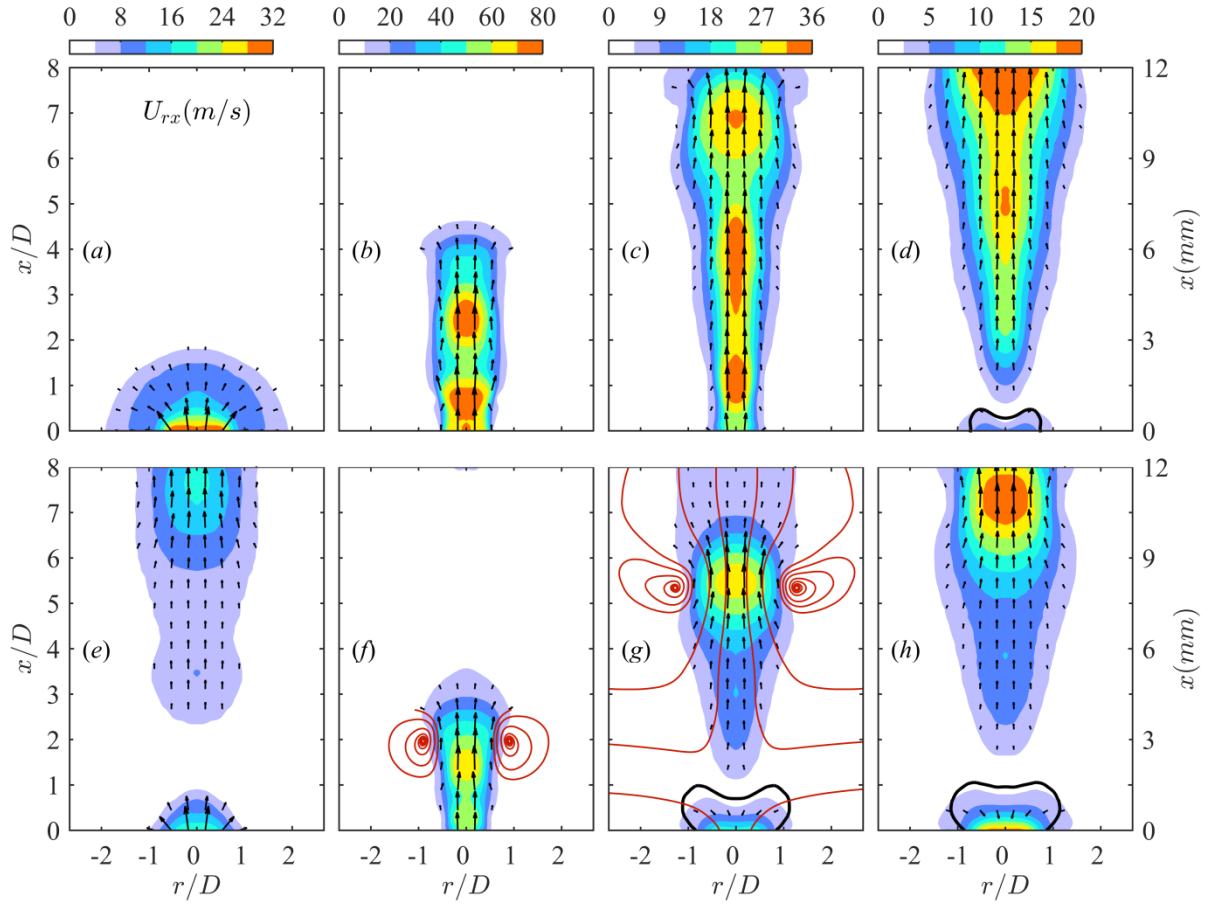


Figure 2. Time evolution of phase-averaged velocity fields at $f^*=0.037$ (Case 1) and $f^*=1.056$ (Case 6). (a) $t=50 \mu\text{s}$, $f^*=0.037$; (b) $t=250 \mu\text{s}$, $f^*=0.037$; (c) $t=500 \mu\text{s}$, $f^*=0.037$; (d) $t=700 \mu\text{s}$, $f^*=0.037$; (e) $t=50 \mu\text{s}$, $f^*=1.056$; (f) $t=250 \mu\text{s}$, $f^*=1.056$; (g) $t=500 \mu\text{s}$, $f^*=1.056$; (h) $t=700 \mu\text{s}$, $f^*=1.056$. Magnitude and direction of U_{rx} are indicated by contours and velocity vectors, respectively. Solid black lines are velocity contour lines of $U_x=-1 \text{ m/s}$.

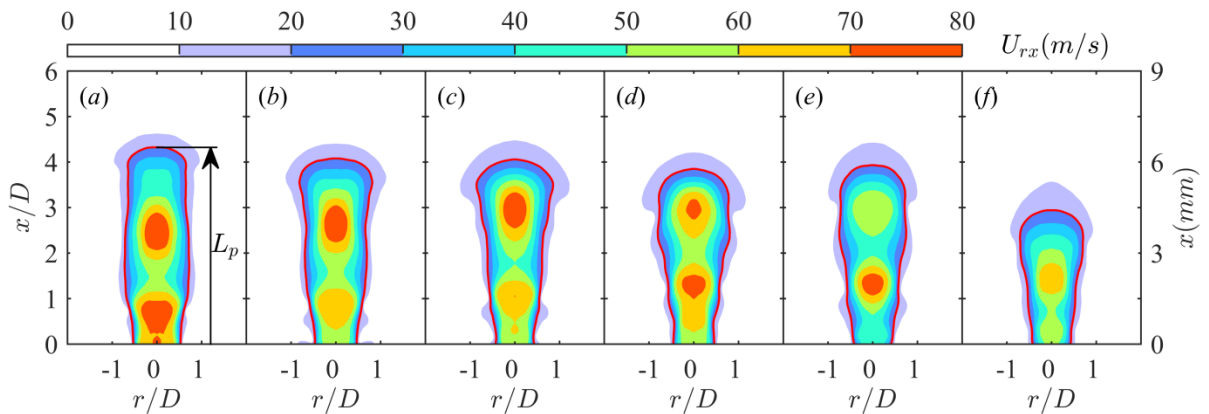


Figure 3. Phase-averaged velocity contours at $t=250 \mu\text{s}$ for increasing frequency. (a) $f^*=0.037$; (b) $f^*=0.074$; (c) $f^*=0.148$; (d) $f^*=0.370$; (e) $f^*=0.739$; (f) $f^*=1.056$; Red lines are velocity contour lines of $U_{rx}=20 \text{ m/s}$.

In comparison to the low-frequency operation, the bow-shape shock waves in Case 6 are limited to the near-exit region at $t=50 \mu\text{s}$ and flooded by the residual jet flow of previous pulses. A relatively weak pulsed jet with 60 m/s peak velocity is issued at $t=250 \mu\text{s}$, followed by an early yet strong suction flow emerging at approximately $t=500 \mu\text{s}$. Only one high-velocity core can be observed in Figure 2 (f)

and (g), indicating a reduced amount of other shear-layer vortices. The peak suction velocity exhibited at $t=700\mu\text{s}$ (15 m/s) is three times higher than the respective peak suction velocity for low frequency operation (Case 1, $f^*=0.037$).

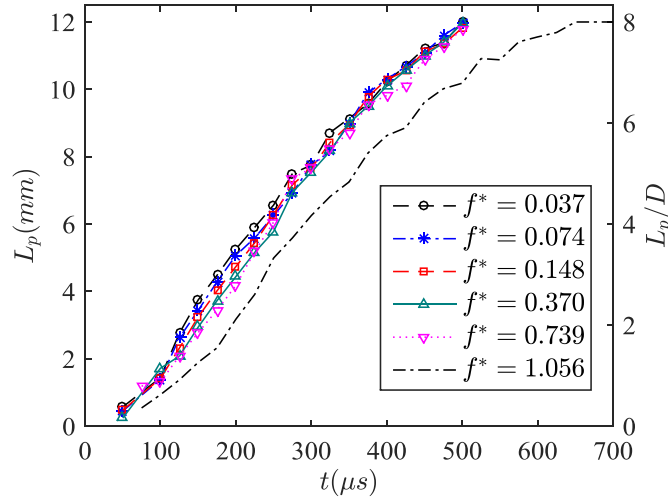


Figure 4. Time evolution of jet penetration length for increasing frequency

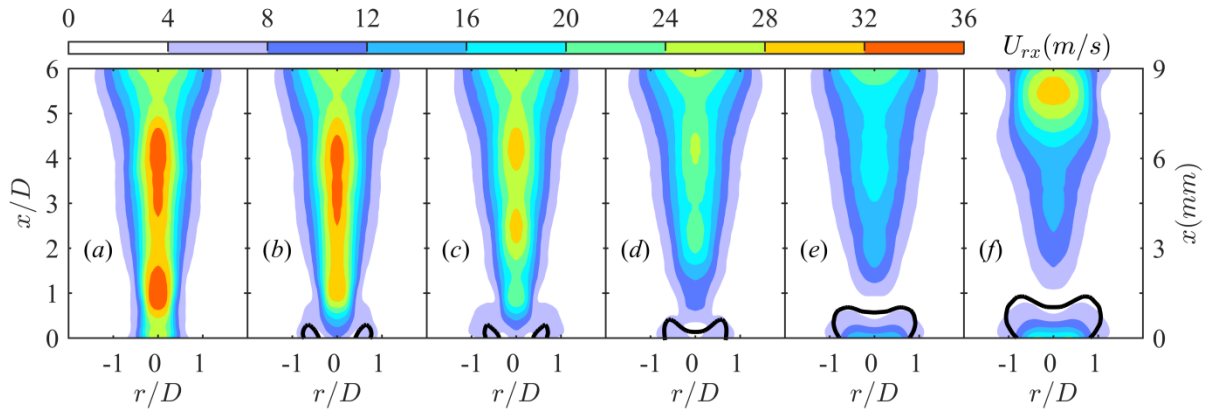


Figure 5 Phase-averaged velocity contours at $t=500\mu\text{s}$ for increasing frequency; (a) $f^*=0.037$; (b) $f^*=0.074$; (c) $f^*=0.148$; (d) $f^*=0.370$; (e) $f^*=0.739$; (f) $f^*=1.056$; Solid black lines are velocity contour line of -1 m/s.

The two major modifications resulting from high-frequency operation are weakened jet and intensified suction. Jet penetration length and exit velocity will be exploited to quantify these modifications. For all tested cases, the velocity contours at $t=250\mu\text{s}$ are shown in Figure 3. As a result, both peak jet velocity and jet penetration differ slightly at $f^*\leq 0.739$ and drop significantly afterwards. The jet penetration length (L_p) is defined arbitrarily as the farthest propagation position of the 20 m/s velocity contour line (Zong & Kotsonis, 2017a), as sketched in Figure 3 (a). The evolution of L_p with time for increasing frequency is shown in Figure 4. As evidenced, a steady increase of L_p is exhibited and the general trend agrees well with that shown in Zong & Kotsonis (2017a). For $f^*\leq 0.739$, all the curves collapse well except for the interval of $100\mu\text{s} < t < 300\mu\text{s}$ where L_p drops monotonically with increasing frequency. Nevertheless, these discrepancies are alleviated in later evolution. When f^* increases from 0.739 to 1.056, a sharp drop of L_p (on average, $1D$) is experienced. This abrupt drop is also evidenced in Figure 3 and mainly related to the enhanced suction flow, which will be quantified later on.

Phase-averaged velocity contours at $t=500 \mu s$ for increasing frequency are shown in Figure 5. The sequence exemplifies how the jet and suction flows alternate. Initially, the air at the exit periphery is ingested into the throat while the air near the exit core region is still being ejected. As the jet flow diminishes, the suction flow expands inwards, gradually occupying the entire exit. Finally, a saddle flow pattern takes shape where the jet and suction flow reside in the near-field and far-field respectively, divided approximately by $x/D=1$ (see Figure 2 (g)). The exit velocity profiles (only U_x component) are further extracted from Figure 5 (a)-(f) and shown in Figure 6 (a). These curves exhibit consistently bell shapes, and suction velocity profiles are significantly fuller than jet velocity profiles. Assuming that the jet induced flow is axisymmetric, the spatially-averaged exit velocity (U_{ex}) can be defined as follows (Zong & Kotsonis, 2017c),

$$U_{ex}(t) = \frac{\int_0^{D/2} U_x(r,t) \pi r dr}{\pi D^2 / 4} \quad (3)$$

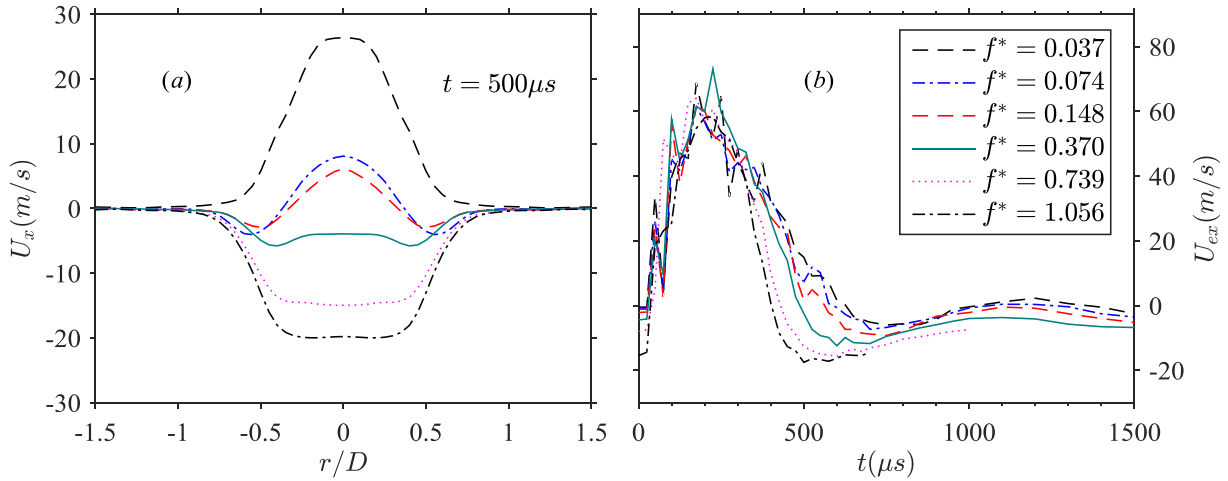


Figure 6 (a) Comparison of exit velocity profiles at $t=500 \mu s$; (b) Time evolution of area-averaged exit velocity for different cases.

The time evolution of U_{ex} for all the tested cases is shown in Figure 6 (b). Positive and negative signs of U_{ex} indicate jet and refresh stages respectively. In the primary jet stage, U_{ex} shows initially a sharp increase, then small-amplitude oscillations around its peak value, and finally a slow linear drop. Peak values of U_{ex} (denoted as U_p) are reached between $t=200 \mu s$ and $t=300 \mu s$, ranging between 58 m/s and 73 m/s for the different frequency cases. Additionally, based on the sign change of U_{ex} , the jet duration time (T_{jet}) can be estimated. With increasing frequency, T_{jet} drops monotonically from 627 μs to 402 μs whereas the peak suction velocity (denoted as U_s) experiences a triple increase from -6 m/s to -18 m/s. For all the tested cases, peak jet and suction velocity and jet duration time are listed in Table 2. In the case of $f^*=0.037$, a weak second jet stage (peak velocity: 2.3 m/s) appears between $t=1100-1300 \mu s$. By contrast, the exit velocity for cases of $f^*\geq 0.074$ never restores back to positive values after $t=T_{jet}$, indicating the absence of multiple alternations between jet and refresh stages at high-frequency repetitive operation (Zong & Kotsonis, 2016a).

Table 2. Peak velocity, jet duration time and mean cavity density

| f^* | $U_p (m/s)$ | $U_s (m/s)$ | $T_{jet} (\mu s)$ | L_e / D | L_s / D | ρ_{ca1} / ρ_0 | ρ_{ca2} / ρ_0 |
|-------|-------------|-------------|-------------------|-----------|-----------|-----------------------|-----------------------|
| 0.037 | 68.8 | -6.0 | 627 | 12.8 | 12.5 | 97.7 % | 97.8 % |
| 0.074 | 61.3 | -7.3 | 588 | 12.0 | 10.4 | 87.0 % | 87.0 % |
| 0.148 | 61.6 | -9.2 | 563 | 11.6 | 8.8 | 75.6 % | 75.4 % |
| 0.370 | 73.1 | -12.4 | 488 | 12.1 | 6.2 | 51.7 % | 51.6 % |
| 0.739 | 64.1 | -15.7 | 430 | 10.8 | 4.4 | 40.9 % | 41.1 % |
| 1.056 | 58.4 | -17.6 | 402 | 9.3 | 3.2 | 34.9 % | 34.2% |

At $f^*=1.056$, it is striking to notice that the initial exit velocity at $t \leq 25 \mu s$ are negative values (-15 m/s) that are much higher than other cases (less than -7 m/s). This indicates that the jets in Case 6 ($f^*=1.056$) ensue while there's still a strong refresh stage (suction) from the previous pulse. This adverse suction flow obstructs the axial propagation of pulsed jets, leading to a reduction of the penetration length as shown in Figure 4.

B. Mean cavity density and cavity temperature

Since the time-evolution of the exit velocity in a complete cycle is resolved, the mean cavity density during quasi-steady working state (ρ_{ca}) can be estimated using the law of mass flow conservation. Two approaches proposed by Zong & Kotsonis (2017c) can be used to calculate this. The first method assumes that the expelled gas mass in one cycle is relatively small compared to the initial cavity gas mass (less than 5%). Based on this assumption, the normalized mean cavity density (ρ_{ca}/ρ_0) can be approximated by the ratio of suction length (L_s) to ejection length (L_e) as shown in Equation (4) where U_{ex}^- and U_{ex}^+ represent positive and negative portion of U_{ex} respectively.

$$\frac{\rho_{ca}}{\rho_0} = \frac{L_s}{L_e} = \frac{\int_0^{T_d} U_{ex}^-(t) dt}{\int_0^{T_d} U_{ex}^+(t) dt} \quad (4)$$

The second method employs a reduced analytical model to simulate the repetitive working process of PSJA and seeks for an optimal initial cavity density satisfying the law of mass flow conservation. With this method, the temporal evolution of both cavity density and exit density can be computed. For all the tested cases, the mean cavity density computed with the aforementioned two methods (distinguished by subscripts, ρ_{ca1}/ρ_0 and ρ_{ca2}/ρ_0) and nondimensional ejection/suction lengths are listed in Table 2. The two methods give comparable results with maximum relative deviation of less than 0.7%. The peak values of L_e/D and L_s/D are very close, being 12.8 and 12.5 respectively. With increasing frequency, both L_e/D and L_s/D decline monotonically. However, the declining rate of the suction length is significantly less than the rate of the ejection length, leading to a reduced mean cavity density.

Since the peak jet velocity for all cases is less than 80 m/s, the absolute cavity pressure (p_{ca}) is expected to vary between 101-105 kPa (Bernoulli principle, $p_{ca} \approx P_0 + (\rho U_{ex})^2/2$). Taking a mean cavity pressure (p_{ca}) of 103 kPa, the mean cavity temperature in the steady working stage (T_{ca}) can be estimated by the ideal gas law, $T_{ca} = p_{ca}/(\rho_{ca}R)$, where R is the gas constant. The variation of T_{ca} and ρ_{ca}

(method 2) with f^* is shown in Figure 7. Below $f^*=0.037$, the mean cavity density at steady working stage is above 97% of the ambient density, indicating negligible frequency effects. As frequency increases, the normalized cavity density drops sharply between $0.037 \leq f^* \leq 0.370$ and slows down afterwards. At $f^*=1.056$, the mean cavity density remains only 1/3 of the ambient density, which corresponds to mean cavity gas temperature of 860K. The high-temperature low-density feature of the cavity gas is mainly caused by the continuous heat accumulation in the transient working stage (Zong et al. 2015b), which will be elucidated later on in Section IV.

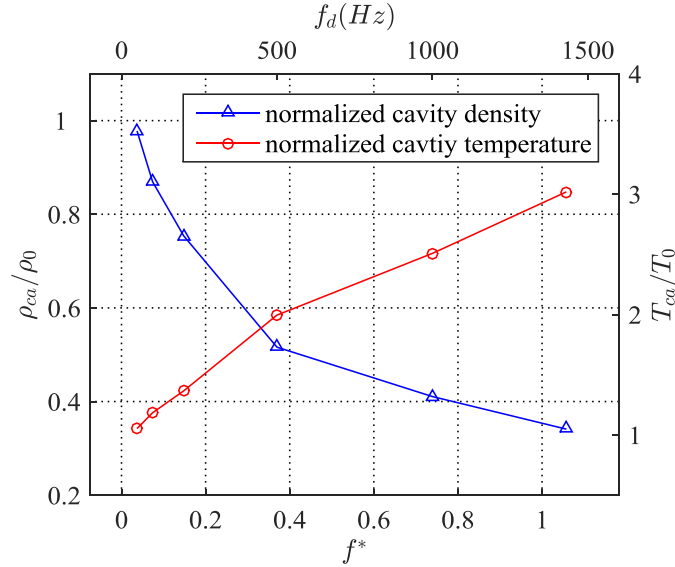


Figure 7 Effect of frequency on normalized mean cavity density and temperature at steady working stage

C. Expelled gas mass, impulse and issued mechanical energy

The combination of time-varying exit velocity and exit density (not shown) enables the evaluation of the cumulative expelled gas mass (M_{ce}), impulse (I_{cp}) and issued mechanical energy (E_{cm}) as shown in Equation (5) (Zong & Kotsonis, 2017).

$$\begin{cases} M_{ce}(t) = \int_0^t \rho_e(s) U_{ex}(s) A_e \cdot ds \\ I_{cp}(t) = \int_0^t U_{ex}(s) \cdot \rho_e(s) |U_{ex}(s)| A_e \cdot ds \\ E_{cm}(t) = \int_0^t 0.5 \cdot U_{ex}^2(s) \cdot \rho_e(s) |U_{ex}(s)| A_e \cdot ds \end{cases} \quad (5)$$

The total expelled gas mass (M_e), total impulse (I_e) and total issued mechanical energy (E_m) pertaining to single pulsed jet are defined as follows,

$$\begin{cases} M_e = M_{ce}(T_{jet}) \\ I_p = I_{cp}(T_d) \\ E_m = E_{cm}(T_d) \end{cases} \quad (6)$$

Using these three integral parameters to normalize the three cumulative parameters shown in Equation (5), another three nondimensional quantities (\bar{M}_{ce} , \bar{I}_{cp} and \bar{E}_{cm}) can be derived as follows.

$$\begin{cases} \overline{M}_{ce}(t) = M_{ce}(t) / M_e \\ \overline{I}_{cp}(t) = I_{cp}(t) / I_p \\ \overline{E}_{cm}(t) = E_{cm}(t) / E_m \end{cases} \quad (7)$$

For all the tested cases, the evolution in time of these three nondimensional quantities (generalized as \overline{X}_{ci}) in one cycle is shown in Figure 8 in order to identify the respective contribution of the jet and refresh stages. Observing the slope of the curve in Figure 8 (a), the averaged mass flow rate in the primary jet stage is demonstrated to be significantly higher than that in the refresh stage at $f^*=0.037$ due to a small jet duty cycle (defined as T_{jet}/T_d , $D_c \approx 0.03$). As the dimensionless frequency increases, D_c increases rapidly and exceeds 0.5 at $f^*=1.056$, indicating that the averaged mass flow rate in the refresh stage has overtaken that in the jet stage. In Figure 8(b), the refresh stage contributes negatively to the total jet impulse yielded in one cycle. At $f^* < 0.148$, the proportion of this negative contribution is negligible (less than 10%). As frequency increases, this negative effect grows. In the cases of $f^*=1.056$, 33% of the jet impulse produced in primary jet stage is counteracted by the suction flow. \overline{E}_{cm} bears a monotonic increase throughout one cycle. The contribution of the refresh stages to the total issued mechanical energy grows with increasing frequency, reaching 9.5% at $f^*=1.056$.

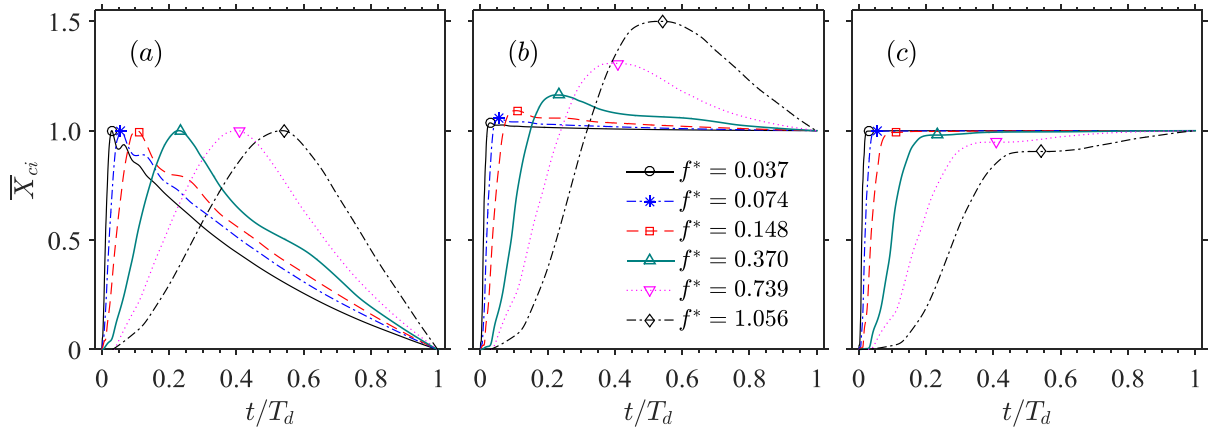


Figure 8. Time evolution of \overline{X}_{ci} in one cycle for all the tested cases; (a) \overline{M}_{ce} ; (b) \overline{I}_{cp} ; (c) \overline{E}_{cm} ; The symbol on each curve is located at $t=T_{jet}$, separating primary jet stage from refresh stage.

M_e and I_p can further be normalized by the initial mass of cavity gas ($\rho_0 V_{ca}$) and the maximum convertible impulse $\sqrt{2E_c \cdot (\rho_0 V_{ca})}$ (Zong & Kotsonis, 2016b; Anderson & Knight, 2012), resulting in nondimensional expelled gas mass (M_e^*) and nondimensional impulse (I_p^*). Additionally, the ratio of E_m to E_c defines the total efficiency of the PSJA (η_t). For all the tested cases, these parameters are listed in Table 3. The peak value of M_e^* is only 4.1%, indicating a relative small variation of cavity density in one cycle. The nondimensional impulse and the total efficiency are on the order of 0.1% and 0.01% respectively, which are consistent with that reported in Zong & Kotsonis (2016b).

The variations of M_e^* , I_p^* and η_t at increasing frequency are further shown in Figure 9. Similar to the trend of mean cavity density observed in Figure 7, M_e^* , I_p^* and η_t decrease monotonically with increasing frequency. The declining rate of M_e^* and I_p^* agrees well at $f^* < 0.370$ however differs slightly afterwards, which can be attributed to the enhanced negative contribution of the suction flow to the jet impulse. For η_t , a relatively slow drop is experienced at $f^* > 0.148$. Compared to Case 1 ($f^*=0.037$) where sufficient time is provided for recovery, the high-frequency operation at $f^*=1.056$ demonstrates 3.9, 5.3 and 3.3 times reduction in M_e^* , I_p^* and η_t , respectively. The product of

discharge frequency and impulse gives the time-averaged thrust produced by the PSJA (F_p). F_p first increases and then drops with f^* , reaching a peak value of 0.544 mN at $f^*=0.739$. This observation is consistent with the total pressure measurement results in Zong et al. (2015b).

Table 3. Integral parameters pertaining to PSJ at steady working stage

| f^* | M_e^* | $I_p(\mu N \cdot s)$ | $I_p^*(\%)$ | $F_p(mN)$ | $E_m(\mu J)$ | $\eta_i(\%)$ |
|-------|---------|----------------------|-------------|-----------|--------------|--------------|
| 0.037 | 4.14 % | 1.65 | 0.27 | 0.082 | 41.2 | 0.0206 |
| 0.074 | 3.50 % | 1.34 | 0.22 | 0.134 | 32.8 | 0.0164 |
| 0.148 | 2.95 % | 1.15 | 0.18 | 0.229 | 30.4 | 0.0152 |
| 0.370 | 2.09 % | 0.86 | 0.14 | 0.428 | 27.5 | 0.0137 |
| 0.739 | 1.47 % | 0.54 | 0.09 | 0.544 | 19.8 | 0.0099 |
| 1.056 | 1.05 % | 0.31 | 0.05 | 0.441 | 12.6 | 0.0063 |

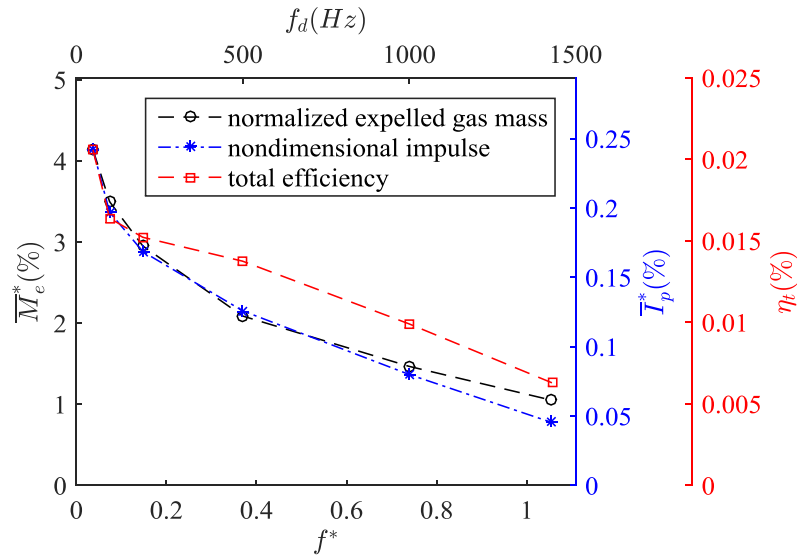


Figure 9. Effect of frequency on nondimensional expelled gas mass, nondimensional impulse and total efficiency

Under the assumption of small expelled gas mass (valid in this paper, <5%) and self-similar exit velocity evolution (i.e. the normalized function of $U_{ex}(t/T_{jet})/U_p$ is identical for different cases), the total expelled gas mass, impulse and jet mechanical energy produced in the primary jet stage are demonstrated to scale with the mean cavity density, jet duration time and increasing orders of peak jet velocity (Zong & Kotsonis, 2017c). When f^* is increased from 0.037 to 1.056, the peak jet velocity changes slightly whereas the mean cavity density and jet duration time are reduced by 2.8 times and 1.6 times respectively. These two factors together account for a theoretical drop of 4.4 times in M_e^* , I_p^* and η_i , which is comparable to the measured values (3.9, 5.3 and 3.3 times). The remaining discrepancy can be ascribed to the influence of suction flow and the assumption of self-similar exit velocity evolution. Overall, the reduced cavity density and shortened jet duration play a dominant role in the performance decline of PSJA at high frequency.

3.2 Time-averaged characteristics in quasi-steady working stage

Based on phase-averaged velocity fields in one period ($U(r, x, t)$), the time-averaged velocity field of PSJ ($\bar{U}(r, x)$) can be constructed using Equation (8), where Δt_i represents the time step between adjacent phases (Zong & Kotsonis, 2017a).

$$\bar{U}(r, x) = \int_0^{T_d} U(r, x, t) dt \approx \frac{1}{T_d} \sum_{i=1}^N U(r, x, t_i) \Delta t_i \quad (8)$$

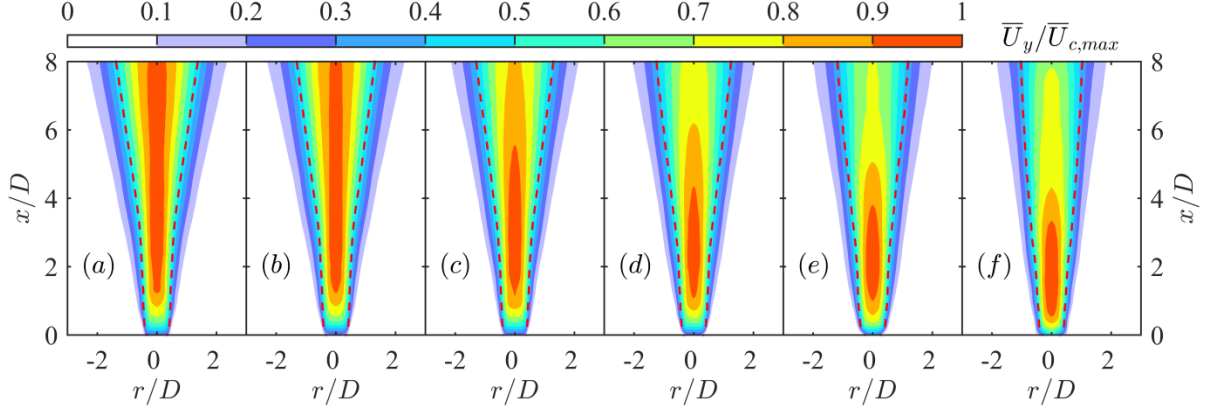


Figure 10 Contours of time-averaged axial velocity for increasing frequency. (a) $f^*=0.037$; (b) $f^*=0.074$; (c) $f^*=0.148$; (d) $f^*=0.370$; (e) $f^*=0.739$; (f) $f^*=1.056$; The red dash lines superimposed on contours are jet boundaries determined by 50% of the jet centreline velocity.

For all the tested cases, contours of time-averaged axial velocity (\bar{U}_y) are shown in Figure 10. The peak centreline velocity (\bar{U}_{cm}) is used to normalize \bar{U}_y , resulting in a range of 0-1. The mean flow of the PSJ is similar to that of steady jets where an expanding jet plume is observed, entraining surrounding fluids during its propagation. No potential core region can be observed and a high-velocity region (defined as $\bar{U}_y / \bar{U}_{cm} > 0.9$) residing approximately $1D$ away from the jet exit is evident. The axial extent of this high-velocity region shrinks from $7D$ to $2D$ when f^* increases from 0.037 to 1.056. The two red dash lines on each contour correspond to the jet boundaries where \bar{U}_y drops to 50% of the jet centreline velocity. The distance between these two dash lines gives the jet width (w_h), which is also known as the full width at half maximum (FWHM; Pope, 2001).

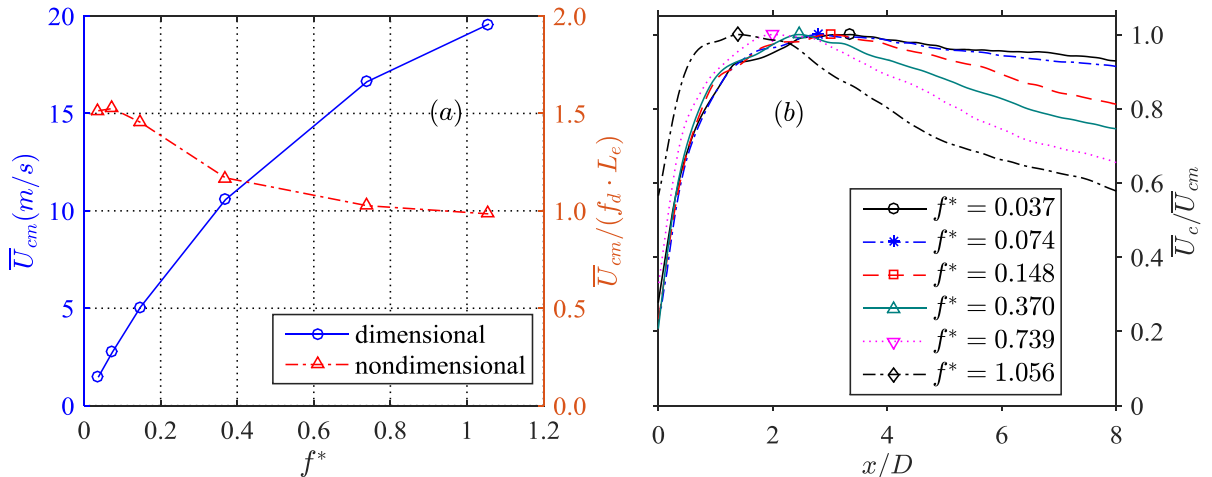


Figure 11. (a) Effect of frequency on peak jet centreline velocity; (b) Axial decay of jet centreline velocity

The variation of the peak centreline velocity (\bar{U}_{cm}) with dimensionless frequency is shown in Figure 11 (a). As expected, \bar{U}_{cm} increases monotonically with frequency, ranging from 1.5 m/s to 20 m/s. The product of discharge frequency and ejection length is used to normalize \bar{U}_{cm} , resulting in a nondimensional peak centreline velocity. For all the tested cases, $\bar{U}_{cm} / (f_d \cdot L_e)$ remains at around 1.5 for low-frequency operation ($f^* < 0.148$) and reduces slowly to 1.0 at high frequency ($f^* > 0.739$). This is consistent with the observation in Zong & Kotsonis (2017c), where the nondimensional peak centreline velocity varies between 1.2-1.6. Figure 11 (b) shows the axial variation of the jet centreline velocity. \bar{U}_c / \bar{U}_{cm} exhibits a non-monotonic change with axial distance. As frequency increases, the peak point moves close to the exit ($x=4D \rightarrow x=2D$), and the decay rate of \bar{U}_c / \bar{U}_{cm} increases which can be ascribed to the decreasing jet momentum.

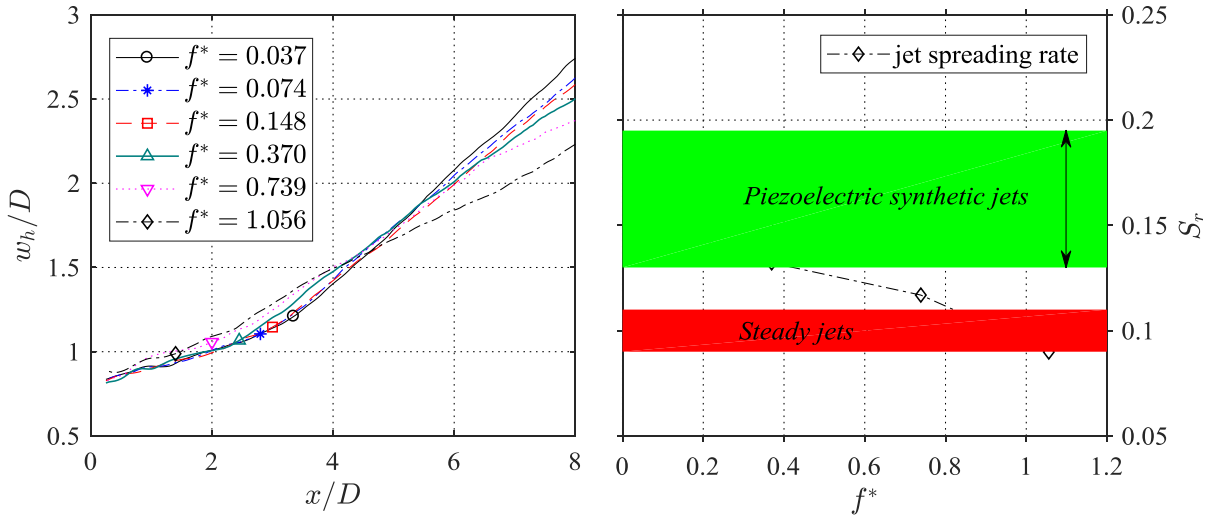


Figure 12. (a) Axial variation of normalized jet width; (b) Jet spreading rate against dimensionless frequency

The axial evolution of the jet width is shown in Figure 12 (a). A steady increase of w_h is experienced. The symbol of each curve denotes the position of the peak jet centreline velocity. These symbols mark notable discontinuities in the slope of the evolution curve, separating each curve into two linear segments. The jet spreading rate (denoted as S_r) determined by the slope of the second segment is shown in Figure 12 (b) ($S_r = 0.5 \cdot d(w_h)/dx$). As a result, the jet spreading rates of the PSJs (0.09-0.17) lie in between the steady jets (0.09-0.11; Hussein et al., 1994; Pope, 2001) and the piezoelectric synthetic jets (0.13-0.195, Shuster & Smith, 2007). With increasing actuation frequency, S decreases monotonically.

The high jet spreading rate at low-frequency cases ($f^* \leq 0.148$) can be ascribed to the front vortex ring (FVR). Specifically, the FVR induced by PSJs is comparable to the sequential vortex rings produced by the piezoelectric synthetic jets. Both of them are considerably larger than the shear layer vortices residing in steady jets (Zong & Kotsonis, 2016a). These large-scale vortex rings entrain rapidly the ambient fluids into the jet core region meanwhile distribute the jet fluids outwards, leading to a fast expansion of the vortex ring size as well as the jet width. Additionally, the entrainment waves created by intermittent termination of the jets also contribute to the high jet spreading rate (Eagle et al. 2014). At high-frequency cases ($f^* \geq 0.739$), those effects are still functioning however the expelled gas mass in one cycle (Me) declines. This declining expelled gas mass contributes negatively to the total

entrained gas mass in one cycle and leads to a decreasing jet spreading rate with increasing frequency. The correlation between M_e and the entrained mass flow is verified as follows.

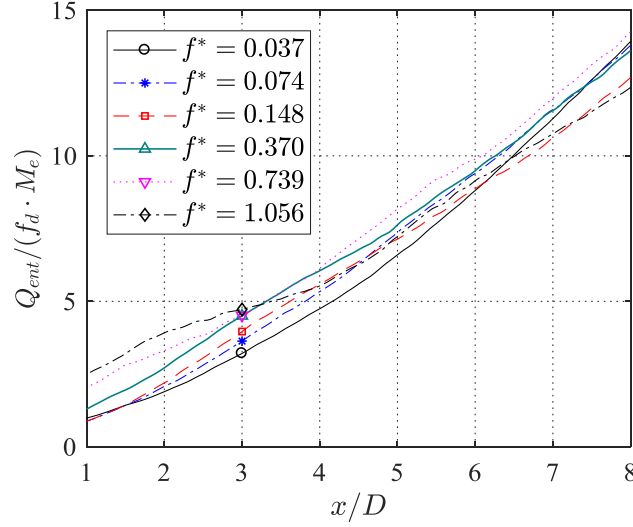


Figure 13 Axial variation of the entrained mass flow for all the tested cases

In our previous work (unpublished, Zong & Kotsonis, 2017c), the entrained mass flow (Q_{ent}) of PSJs are defined in time-averaged velocity fields, and a close relationship between the jet entrainment and the jet spreading is demonstrated using simplified theoretical analysis. Specifically, Q_{ent} is proportional to both the jet centreline velocity (\bar{U}_{cm}) and the square of jet width ($w_h(x)$), provided that the jet velocity profiles at different axial positions are self-similar (not necessarily momentum preserving). Following the same definition, the entrained mass flow at different axial positions for all the tested cases are computed and shown in Figure 13. As a result, Q_{ent} increases approximately linearly with the axial coordinate and collapse reasonably when scaled by $f_d M_e$. As $f_d M_e$ represents the total expelled gas mass per second (exclude suction), the positive correlation between the entrained mass flow and the expelled gas mass per pulse (M_e) is evidenced.

IV. TRANSIENT-STAGE ANALYSIS

Analysis of the quasi-steady stage reveals that under high-frequency operation, the intensity of the pulsed jet can deteriorate significantly compared to that obtained in single-shot mode. Several important parameters are responsible for this deterioration including the reduced cavity density, reduced jet duration and enhanced suction flow. In order to elucidate the origin of these dependencies an analysis of the transient stages of operation, ensuing during the initial few actuation cycles, is performed in this section.

At $f^*=1.056$, the evolution of the phase-averaged exit velocity pertaining to the first 30 pulses is shown in Figure 14. To be noted that the ‘phase’ here (denoted as t_1) refers to the time elapsed after the 1st pulse is ignited, which is different from that used in Section III ($0 \leq t \leq T_d$). For each cycle, the peak jet and suction velocity, as well as the jet duration time are shown in Figure 15. It is striking to notice that no refresh stage is present in the first cycle. Additionally, the peak jet velocity of the first cycle (70.4 m/s) is close to the steady-stage value at $f^*=0.037$ (68.8 m/s) since in both cases the mean cavity density is approximately at the levels of ambient density. During the transient working process, the peak suction velocity shows a steady increases at $N_c \leq 7$ and remains approximately constant at 18

m/s afterwards. For the jet duty cycle (D_c), a sharp drop from 1 to 0.65 is experienced during the first 10 cycles and the steady-stage value (0.57) is not approached until $N_c \geq 20$. The increasing suction velocity and reducing jet duty cycle demonstrate an intensifying suction flow. The peak jet velocity appears unstable in the first 10 pulses as is evident in Figure 15 (a). After $N_c \geq 10$, a mild fluctuation around the steady-stage value (oscillation amplitude: less than 3 m/s) is exhibited. Based on the variations of these three parameters, it is concluded that the exit velocity takes approximately 20 cycles to stabilize, which is consistent with the analytical model results in Zong et al. (2015) and the simulation results in Sary et al. (2014).

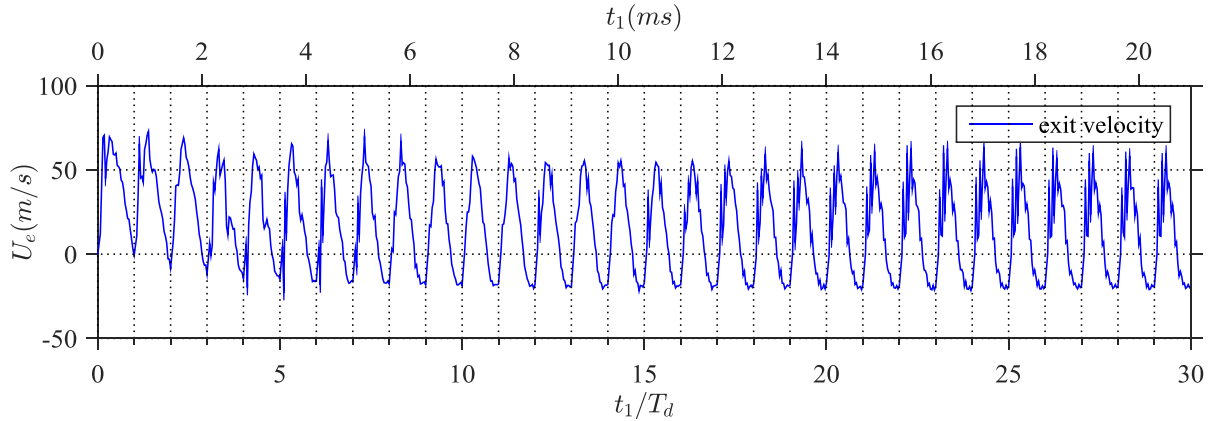


Figure 14 Time evolution of the exit velocity pertaining to the first 30 pulses at $f^*=1.056$.

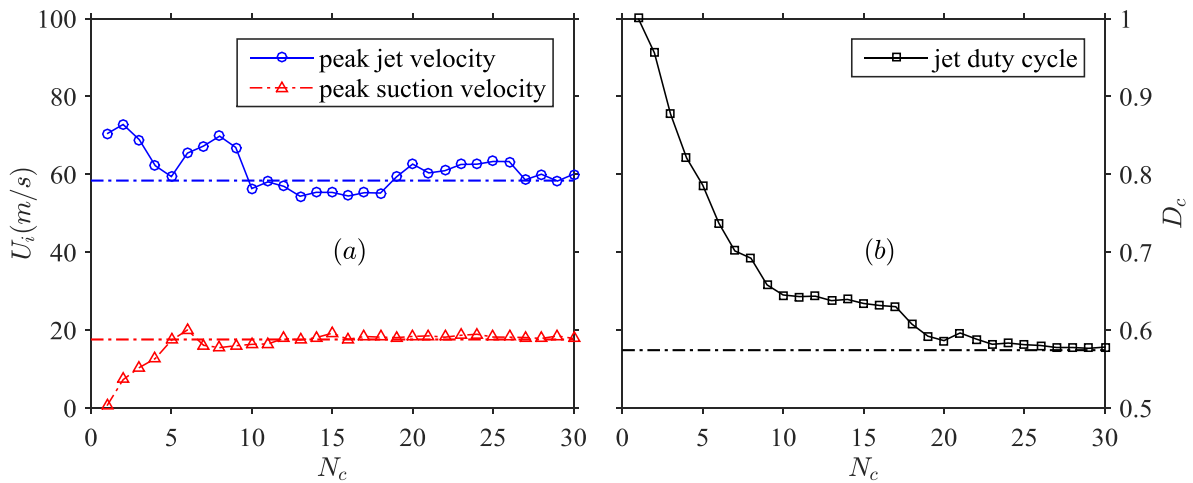


Figure 15 Evolution of jet performance parameters with cycle number (N_c) in transient stage at $f^*=1.056$. (a) Peak jet and suction velocity; (b) Jet duty cycle. The steady-stage values of these performance parameters are indicated by dot-dash lines.

Based on the exit velocity shown in Figure 14, the temporal variation of the cavity density in the transient stage can be computed using the model proposed by Zong & Kotsonis (2017c). Following the same assumption made in Section 3.1.B (mean cavity pressure: 103 kPa), the mean cavity temperature as a function of the elapsed cycles can be estimated. Figure 16 shows the variation of ρ_{ca} and T_{ca} pertaining to the first 200 pulses. Although the exit velocity already exhibits periodic variation after 20 cycles (Figure 14), the mean cavity density and temperature are not stabilised until $N_c=129$ (convergence criterion: relative variation < 5%). The slow convergence rate can be attributed to the low

value of expelled gas mass (<5%) which limits the mass exchange between the actuator cavity and the outer environment.

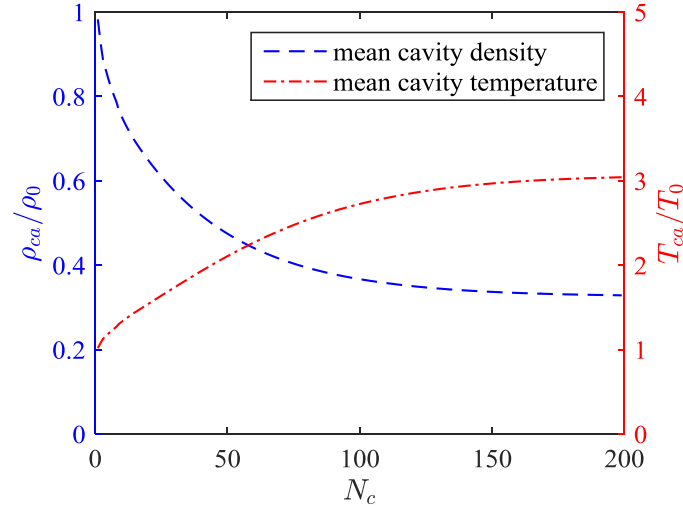


Figure 16 Variation of mean cavity density and temperature during transient stage at $f^*=1.056$

The mean cavity temperature shows a steady increase with the cycle number (N_c), due to the continuous heat accumulation in the cavity during the transient stage. This increasing cavity temperature further affects the variation of the jet duration time. Anderson & Knight (2012) indicated that the dimensionless jet duration time (T^*) depends solely on the nondimensional energy deposition (ε), regardless of the flow status in the actuator throat (sonic or subsonic).

$$T^* = \frac{T_{jet} A_e \sqrt{\gamma R T_{ca}}}{V_{ca}} = g(\varepsilon) \quad (9)$$

Therefore, with constant energy deposition and increasing mean cavity temperature as is the case for transient stage, the jet duration time will decrease which is consistent with the observation in Figure 15 (b).

V. ENERGY EQUILIBRIUM ANALYSIS IN ONE CYCLE

Once the PSJA reaches the quasi-steady working stage, the mean cavity temperature will remain constant and energy conservation should be satisfied in one cycle. Starting from the energy conservation law, a relationship between steady cavity temperature and working frequency can be established. In a thermodynamic framework, the actuator cavity can be considered as an open system, exchanging both energy and mass with the surroundings. The first law of thermodynamics for the considered system is written as follows,

$$E_h - E_{ex} - E_{diss} = W \quad (10)$$

E_h is the heating energy, which is much smaller than the capacitor energy (E_c) due to inevitable energy losses on wire parasitic resistance and in gas ionization processes; E_{diss} represents the heat dissipation term caused by convection and radiation. E_{ex} is the heat exchange brought by the mass exchange between actuator and external environment, since the air issued and ingested are of different temperature. W stands for the cycle work. Under the assumption that the energy deposition stage, jet

stage and refresh stage are constant-volume heating process, isentropic expansion process and constant pressure cooling process respectively, the cycle work and the heat exchange term can be estimated by Equations (11)-(12) where ε_h denotes the ratio of heating energy to the initial internal energy of the cavity gas, E_h/E_g (Zong et al., 2016).

$$W = E_g[(1 + \varepsilon_h) - (1 + \varepsilon_h)^{1/\gamma}] \quad (11)$$

$$E_{ex} = C_v \Delta m (T_{ca} - T_0) = E_g [1 - (1 + \varepsilon_h)^{-1/\gamma}] (1 - \frac{T_0}{T_{ca}}) \quad (12)$$

Under the condition of small ε_h (less than 0.5), Equation (11)-(12) can be further simplified using first-order approximation,

$$W \approx (1 - 1/\gamma) \varepsilon_h E_g \quad (13)$$

$$E_{ex} \approx \frac{1}{\gamma} (1 - \frac{T_0}{T_{ca}}) \varepsilon_h E_g \quad (14)$$

Since the the heat capacity of the ceramic cavity shell is far beyond that of the cavity gas (approximately 10^4 times), a negligible temperature increase will be experienced by the ceramic shell during short-time operation (4 K for less than 200 pulses). Thus, the heat dissipation term can be written as follows.

$$E_{diss} = h_c S_{in} (T_{ca} - T_0) / f_d + k_{emi} k_{abs} \sigma S_{in} (T_{ca}^4 - T_0^4) / f_d \quad (15)$$

Where h_c is the convective heat transfer coefficient (typical value for PSJA: 100 W/[K·m²], Zong et al. 2015b). S_{in} represents the area of the cavity internal surface. σ is the Stefan–Boltzmann constant. k_{emi} and k_{abs} stand for the emissivity of the cavity gas and the absorptivity of the ceramic shell respectively. k_{emi} depends on the chemical composition of the gas (CO₂, H₂O et al.) and is estimated to be less than 0.01 for the tested cases (modelled as humid air due to seeding, reference pressure: 1 atm; reference length: 0.01 m) (Brewster, 1992). In the range of 300K < T_{ca} < 900K, the ratio of radiative heat term to convective heat term in Equation (13) is computed to be less than 0.03, indicating negligible radiative heat transfer between the ceramic shell and the cavity gas. Substituting Equations (13)-(15) to Equation (10), the relationship between the mean cavity temperature/ density and discharge frequency can be derived as shown in Equation (16).

$$\begin{cases} \frac{\rho_{ca}}{\rho_0} = \frac{T_0}{T_{ca}} = \frac{2}{1 + \sqrt{1 + 4(2 - \sqrt{2})f_d / f_c}} \\ f_c = \frac{(2 - \sqrt{2})h_c \gamma S_{in} T_0}{E_h} \end{cases} \quad (16)$$

As a result, the mean cavity density is inversely proportional to the square root of f_d / f_c . f_c is termed as a thermal cut-off frequency, quantifying the ratio of convective heat transfer rate to heat addition rate. The coefficient is chosen as $(2 - \sqrt{2})$ such that ρ_{ca} / ρ_0 is reduced to 0.707 (3 dB) when $f_d / f_c = 1$. With an unchanged heating energy, f_c is positively proportional to the convective heat transfer coefficient and the area of cavity internal surface. By contrast, when h_c and S_{in} remain constant, f_c reduces with increasing heating energy.

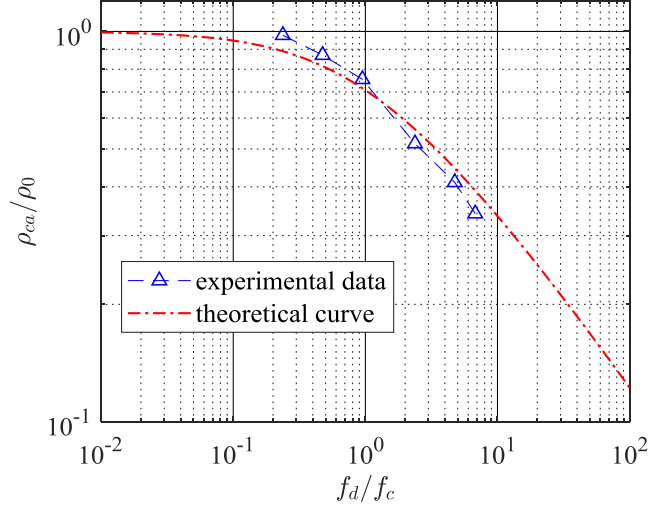


Figure 17 Comparison between theoretical and experimental cavity density at increasing frequency

Using Equation (16) to fit the experimental data shown in Figure 7, a good agreement is obtained as shown in Figure 17. The fitting value of f_c is 210 Hz. Below $0.1f_c$, the cavity density is close to ambient density and the frequency effect can be neglected. Beyond f_c , a significant drop of cavity density is exhibited which is detrimental to the repetitive performance of PSJA. To obtain a higher value of f_c , the actuator cavity should be properly designed to accelerate the heat exchange between the cavity shell and the cavity gas. For example, slender cavities with large height-to-diameter ratio are recommended to increase the area of internal surface at a fixed cavity volume; Sharp corners in the actuator cavity should be avoided to improve the recirculation of internal flow, thus to increase the overall convective heat transfer coefficient. Additionally, for the same actuator geometry, large energy deposition will result in a fast decay of cavity density with increasing frequency. This fast declining cavity density can be further propagated into the three integral parameters (expelled gas mass, jet impulse and jet mechanical energy). Thus, to maintain a relatively high repetitive performance of the PSJA, the input energy should also be limited.

Revisiting Figure 7, the trend of increasing cavity temperature with increasing frequency can be interpreted from the perspective of energy equilibrium. Specifically as the frequency goes up, the energy deposited in the cavity increases linearly. According to the second law of thermodynamics (Equation (10)), the difference between the energy deposited and the cycle work done to the external environment must be dissipated to a heat sink (namely the surrounding air). The heat dissipation rate is related to both the heat transfer coefficients and the temperature difference between the cavity gas and the ambient air ($T_{ca}-T_0$, Equation (15)). Consequently, for unchanged heat transfer coefficients, the mean cavity temperature at the steady stage (T_{ca}) has to increase with the actuation frequency to meet the energy equilibrium in the actuator cavity.

VI. CONCLUSIONS

The influence of dimensionless frequency (discharge frequency over Helmholtz natural frequency, f_d/f_h) on several performance characteristics of a two-electrode PSJA is investigated in a wide range from $f^*=0.037$ to $f^*=1.056$, by virtue of a high-speed planar PIV system.

When the PSJA reaches steady working status, the spatially-averaged exit velocity experiences a periodical evolution in time, reaching a peak value shortly after the discharge. The jet penetration

length (L_p) differs slightly at $f^* \leq 0.739$ whereas declines noticeably afterwards. As frequency increases, the jet duration time (T_{jet}) drops monotonically, whilst the peak suction velocity (U_s) rises from -6 m/s to -17.6 m/s. This enhanced suction flow is responsible for the declining jet penetration. Three crucial integral parameters including the expelled gas mass (M_e^*), impulse (I_p) and issued mechanical energy (E_m) are estimated using a reduced-order model. As the dimensionless frequency increases from 0.037 to 1.056, M_e^* , I_p and E_m exhibit 3.9, 5.3 and 3.3 times reduction respectively, which are mainly caused by the reduced cavity density at high frequency operation. Within one actuation cycle, the mean mass flow rate at the refresh stage is initially less than the jet stage for cases with low dimensionless frequency, however catches up by $f^* \geq 0.739$. Additionally, the impulse produced by the jet expulsion is partially counteracted by the inevitable suction flow. The proportion that is cancelled is initially less than 10% and grows to 33% at $f^* = 1.056$.

The time-averaged jet centreline velocity (\bar{U}_c) changes non-monotonically with the axial coordinate (x -coordinate). The peak centreline velocity normalized by $f_d L_e$ remains at around 1.5 for low-frequency operation ($f^* < 0.148$) and drops slowly to 1.0 afterwards. Peak values of \bar{U}_c are reached between $1 < x/D < 4$, and the decay rate of \bar{U}_c increases with discharge frequency. The jet spreading rate of the PSJ, determined from the slope of w_h , ranges from 0.09 to 0.14, which is much higher than the steady jets. During the transient working stage of the PSJA at $f^* = 1.056$, the exit velocity trace elapses 20 cycles to stabilize. In comparison to the relatively fast convergence of the exit velocity, approximately 130 cycles are needed for the mean cavity density/temperature to reach steady values, which is caused by the small expelled gas mass (5%). The energy equilibrium analysis of the cavity gas in one cycle shows that the mean cavity density decreases monotonically with the square root of discharge frequency, and the declining rate is governed by a thermal cut-off frequency (f_c , 210Hz for the current study). f_c is directly proportional to the convective heat transfer coefficient between actuator shell and cavity gas, as well as the area of cavity internal surface. A high value of f_c corresponds to a slow decay of mean cavity density in high-frequency operation.

REFERENCE

- Anderson, K. V., & Knight, D. D. (2012). Plasma jet for flight control. *AIAA Journal*, 50(9), 1855-1872.
- Belinger, A., Hardy, P., Barricau, P., Cambronne, J. P., & Caruana, D. (2011). Influence of the energy dissipation rate in the discharge of a plasma synthetic jet actuator. *Journal of Physics D: Applied Physics*, 44(36), 365201.
- Belinger, A., Naudé, N., Cambronne, J. P., & Caruana, D. (2014). Plasma synthetic jet actuator: electrical and optical analysis of the discharge. *Journal of Physics D: Applied Physics*, 47(34), 345202.
- Brewster, M. Q. (1992). Thermal radiative transfer and properties. John Wiley & Sons.
- Cattafesta III, L. N., & Sheplak, M. (2011). Actuators for active flow control. *Annual Review of Fluid Mechanics*, 43, 247-272.
- Chedevergne, F., Léon, O., Bodoc, V., & Caruana, D. (2015). Experimental and numerical response of a high-Reynolds-number $M = 0.6$ jet to a Plasma Synthetic Jet actuator. *International Journal of Heat and Fluid Flow*, 56, 1-15.
- Chiatto, M., & de Luca, L. (2017). Numerical and experimental frequency response of plasma synthetic jet actuators. In *55th AIAA Aerospace Sciences Meeting* (p. 1884).
- Corke, T. C., Enloe, C. L., & Wilkinson, S. P. (2010). Dielectric barrier discharge plasma actuators for flow control. *Annual review of fluid mechanics*, 42, 505-529.

- Cybyk, B., Grossman, K., & Van Wie, D. (2003, June). Computational assessment of the sparkjet flow control actuator. In *33rd AIAA Fluid Dynamics Conference and Exhibit* (p. 3711).
- de Luca, L., Girfoglio, M., & Coppola, G. (2014). Modeling and experimental validation of the frequency response of synthetic jet actuators. *AIAA Journal*, 52(8), 1733-1748.
- Eagle, W. E., Musculus, M. P., Malbec, L. M. C., & Bruneaux, G. (2014, May). Measuring transient entrainment rates of a confined vaporizing diesel jet. In *ILASS Americas 26th Annual Conference on Liquid Atomization and Spray Systems*, Portland, OR.
- Emerick, T., Ali, M. Y., Foster, C., Alvi, F. S., & Popkin, S. (2014). SparkJet characterizations in quiescent and supersonic flowfields. *Experiments in Fluids*, 55(12), 1–21.
- Golbabaei-Asl, M., Knight, D., & Wilkinson, S. (2014). Novel technique to determine sparkjet efficiency. *AIAA Journal*, 53(2), 501-504.
- Greene, B. R., Clemens, N. T., Magari, P., & Micka, D. (2015). Control of mean separation in shock boundary layer interaction using pulsed plasma jets. *Shock Waves*, 25(5), 495-505.
- Grossman, K., Bohdan, C., & VanWie, D. (2003, January). Sparkjet actuators for flow control. In *41st Aerospace Sciences Meeting and Exhibit* (p. 57).
- Grundmann, S., & Tropea, C. (2007). Experimental transition delay using glow-discharge plasma actuators. *Experiments in Fluids*, 42(4), 653-657.
- Hussein, H. J., Capp, S. P., & George, W. K. (1994). Velocity measurements in a high-Reynolds-number, momentum-conserving, axisymmetric, turbulent jet. *Journal of Fluid Mechanics*, 258, 31-75.
- Narayanaswamy, V., Raja, L. L., & Clemens, N. T. (2010). Characterization of a high-frequency pulsed-plasma jet actuator for supersonic flow control. *AIAA Journal*, 48(2), 297-305.
- Narayanaswamy, V., Raja, L. L., & Clemens, N. T. (2012). Control of unsteadiness of a shock wave/turbulent boundary layer interaction by using a pulsed-plasma-jet actuator. *Physics of Fluids*, 24(7), 076101.
- Pope, S. B. (2001). *Turbulent flows*. Cambridge University Press.
- Post, M. L., & Corke, T. C. (2004). Separation control on high angle of attack airfoil using plasma actuators. *AIAA Journal*, 42(11), 2177-2184.
- Reedy, T. M., Kale, N. V., Dutton, J. C., & Elliott, G. S. (2013). Experimental characterization of a pulsed plasma jet. *AIAA Journal*, 51(8), 2027-2031.
- Samimy, M., Kim, J. H., Kastner, J., Adamovich, I., & Utkin, Y. (2007). Active control of high-speed and high-Reynolds-number jets using plasma actuators. *Journal of Fluid Mechanics*, 578, 305-330.
- Sary, G., Dufour, G., Rogier, F., & Kourtzanidis, K. (2014). Modeling and parametric study of a plasma synthetic jet for flow control. *AIAA Journal*, 52(8), 1591-1603.
- Shuster, J. M., & Smith, D. R. (2007). Experimental study of the formation and scaling of a round synthetic jet. *Physics of fluids*, 19(4), 045109.
- Thomas, F. O., Kozlov, A., & Corke, T. C. (2008). Plasma actuators for cylinder flow control and noise reduction. *AIAA Journal*, 46(8), 1921-1931.
- Wang, L., Xia, Z. X., Luo, Z. B., & Chen, J. (2013). Three-electrode plasma synthetic jet actuator for high-speed flow control. *AIAA Journal*, 52(4), 879-882.
- Wu, J. Z., Ma, H. Y., & Zhou, M. D. (2007). Vorticity and vortex dynamics. *Springer Science & Business Media*.
- Xu, D. A., Shneider, M. N., Lacoste, D. A., & Laux, C. O. (2014). Thermal and hydrodynamic effects of nanosecond discharges in atmospheric pressure air. *Journal of Physics D: Applied Physics*, 47(23), 235202.
- Zhu, Y., Wu, Y., Jia, M., Liang, H., Li, J., & Li, Y. (2014). Influence of positive slopes on ultrafast heating in an atmospheric nanosecond-pulsed plasma synthetic jet. *Plasma Sources Science and Technology*, 24(1), 015007.
- Zong, H., Cui, W., Wu, Y., Zhang, Z., Liang, H., Jia, M., & Li, Y. (2015a). Influence of capacitor energy on performance of a three-electrode plasma synthetic jet actuator. *Sensors and Actuators A: Physical*, 222, 114-121.

- Zong, H, Wu, Y., Li, Y., Song, H., Zhang, Z., & Jia, M. (2015b). Analytic model and frequency characteristics of plasma synthetic jet actuator. *Physics of fluids*, 27(2), 027105.
- Zong, H., & Kotsonis, M. (2016a). Characterisation of plasma synthetic jet actuators in quiescent flow. *Journal of Physics D: Applied Physics*, 49(33), 335202.
- Zong, H., & Kotsonis, M. (2016b). Electro-mechanical efficiency of plasma synthetic jet actuator driven by capacitive discharge. *Journal of Physics D: Applied Physics*, 49(45), 455201.
- Zong, H., & Kotsonis, M. (2017a). Effect of slotted exit orifice on performance of plasma synthetic jet actuator. *Experiments in Fluids*, 58(3), 17.
- Zong, H., & Kotsonis, M. (2017b). Interaction between plasma synthetic jet and subsonic turbulent boundary layer. *Physics of Fluids*, 29(4), 045104.
- Zong, H., & Kotsonis, M. (2017c). Formation, evolution and scaling of plasma synthetic jet. Submitted to *Journal of Fluids Mechanics* (see supplementary materials).
- Zong, H, Wu, Y., Jia, M., Song, H., Liang, H., Li, Y., & Zhang, Z. (2016a). Influence of geometrical parameters on performance of plasma synthetic jet actuator. *Journal of Physics D: Applied Physics*, 49(2), 025504.
- Zong, H., Wu, Y., Song, H., & Jia, M. (2016b). Efficiency Characteristic of Plasma Synthetic Jet Actuator Driven by Pulsed Direct-Current Discharge. *AIAA Journal*, 3409-3420.